Impact of Varying Lidar Measurement and Data Processing Techniques in evaluating Cirrus Cloud and Aerosol Direct Radiative Effects.

S. Lolli[1,2,1], F. Madonna[1], M. Rosoldi[1], J. R. Campbell[3], E. J Welton[4] J. R. Lewis[2], Y. Gu[5], G. Pappalardo[1]

[1] CNR-IMAA, Istituto di Metodologie Ambientali Tito Scalo (PZ), Italy

[2] NASA GSFC-JCET, Code 612, 20771 Greenbelt, MD, USA

[3]Naval Research Laboratory, Monterey, CA, USA

[4]NASA GSFC, Code 612, 20771 Greenbelt, MD, USA

[5]UCLA, University of California Los Angeles, Los Angeles, USA

ABSTRACT

In the past two decades, ground-based lidar networks have drastically increased in scope and relevance, thanks primarily to the advent of lidar observations from space and their need for validation. Lidar observations of aerosol and cloud geometrical, optical and microphysical atmospheric properties are subsequently used to evaluate their direct radiative effects on climate. However, the retrievals are strongly dependent on the lidar instrument measurement technique and subsequent data processing methodologies. In this paper, we evaluate the discrepancies between the use of Raman and elastic lidar measurement techniques and corresponding data processing methods for two aerosol layers in the free troposphere and for two cirrus clouds with different optical depths. Results show that the different lidar techniques are responsible for discrepancies in the model-derived direct radiative effects for biomass burning (0.05 W/m^2 at surface and 0.007 W/m^2 at top of the atmosphere) and dust aerosol layers (0.7 W/m^2 at surface and 0.85 W/m^2 at top of the atmosphere).

[1] Corresponding author: simone.lolli@imaa.cnr.it

Data processing is further responsible for discrepancies in both thin (0.55 W/m^2 at surface and 2.7 W/m^2 at top of the atmosphere) and opaque (7.7 W/m^2 at surface and 11.8 W/m^2 at top of the atmosphere) cirrus clouds. Direct radiative effect discrepancies can be attributed to the larger variability of the lidar ratio for aerosols (20-150 sr) with respect to cirrus clouds (20-35 sr). For this reason, the influence of the applied lidar technique plays a more fundamental role in aerosol monitoring because the lidar ratio must be retrieved with relatively high accuracy. On the contrary, for cirrus clouds, being the lidar ratio much less variable, the data processing is critical because smoothing it modifies the aerosol and cloud vertically resolved extinction profile that is used as input to compute direct radiative effect calculations.

1. Introduction

According to the International Panel for Climate Change (IPCC, 2014), the major sources of uncertainty relating to current climate studies include direct and indirect radiative effects caused by anthropogenic and natural aerosols. Further, current estimates of the global aerosol direct radiative effect remain subject to large relative uncertainties affecting even the actual sign (indicating either net cooling or heating of the earth-atmosphere system), which may change from positive to negative diurnally (e.g., Campbell et al., 2016, Lolli et al., 2017a, Tosca et al., 2017). This depends on the so-called albedo effect (or the capability of aerosols for reflecting incoming solar light) and whether or not it is outweighing the greenhouse effect (or the capability of trapping/absorbing outgoing longwave radiation; Campbell et al., 2016)

Studies on cloud and aerosol optical, geometrical and microphysical properties largely increased in the last two decades through the abundance of passive ground-based measurements (i.e., AErosol RObotic NETwork Network; AERONET Holben et al., 1998, Dubovik et al., 2000, Smirnov et al., 2005, Eck et al., 2014; the Atmospheric Radiation Measurement program; ARM; Campbell et al., 2002, Ferrare et al., 2006, Perez-Ramirez

et al., 2012, McComiskey et al., 2016; Aerosols, Clouds and Trace gases Research Infrastructure; ACTRIS Asmi et al., 2013, Pappalardo et al., 2014) or using satellite sensors (i. e. MODerate resolution Infrared Spectroradiometer; MODIS, Tanré et al., 1997, King et al., 2003, Remer et al., 2005; i. e. Multi-angle Imaging Spectro-Radiometer; MISR, Diner et al., 1998, Di Girolamo et al., 2004, Kahn et al., 2009; i.e. Polarization and Anisotropy of Reflectances for Atmospheric science coupled with Observations from a Lidar; PARASOL, Tanré et al., 2011; NASA Aerosol-Cloud Ecosystem, ACE, Whiteman et al., 2018). Nevertheless, these measurements provide only an estimate of the columnar aerosol (or cirrus cloud) properties.

On the other hand, the Cloud-Aerosol Lidar with Orthogonal Polarization (CALIOP; Winker et al., 2007), on board of the Cloud-Aerosol Lidar and Infrared Pathfinder Satellite Observations (CALIPSO) satellite launched by the National Aeronautics and Space Administration (NASA) in 2006, is capable of estimating range-resolved aerosol and cloud physical properties. However, the sun-synchronous orbit limits spatial and temporal coverage (orbital revisit time period of 16 days) that make the datasets difficult to apply and interpret for specific forms of process study. The vertical structure of cloud and aerosol properties can also be retrieved through combined lidar and radar ground-based measurements as proposed in the frame of the CloudNet European Project (Illingworth et al., 2015). Still, the radar technique proves capable of characterizing only the relatively extreme fraction of the aerosol size distribution (Madonna et al., 2010, Madonna et al., 2013).

Based on the progress in optical technologies in the late 1990's and the beginning of 2000's, federated ground networks of lidars were established [NASA Micro Pulse Lidar NETwork(MPLNET), Campbell et al., 2002, Welton et al., 2002, Lolli et al., 2013; European Aerosol Research LIdar NETwork, (EARLINET) Pappalardo et al., 2014, Asian Dust NETwork (ADNET), Sugimoto et al., 2010, Latin American Lidar NETwork

(LALINET), Antuña-Marrero et al., 2015, Lolli et al., 2015], the bulk of which are based on single or dual-channel elastic and Raman lidar instruments. The Eulerian viewpoint of ground-based lidars is providing important contextual measurements relative to satellite profiling, like from CALIOP (Winker et al., 2007).

The emerging prominence of ground-based lidar, however, strengthens the necessity for further studies of optical, geometrical and microphysical aerosols and clouds properties resolved from multi-spectral lidar techniques, as claimed by several papers (Pappalardo et al., 2004, Mona et al., 2006, Wang et al., 2012, Pani et al., 2016, Lolli et al., 2013, Campbell et al., 2016, Lolli et al., 2017). Multi-spectral and Raman lidars can retrieve aerosol and cloud properties with much better accuracy than elastic lidars, without many fundamental assumptions, (e.g. Ansmann et al., 1992; Goldsmith et al. 1998, Mona et al., 2012, Pappalardo et al., 2014), thought with greater operational expenses. The High Spectral Resolution Lidar (HSRL - Shipley et al., 1983; Grund and Eloranta, 1991) technique allows for the separation of molecular and aerosol signals, and thus affords an independent retrieval of aerosols extinction and backscattering coefficients. However, the technology remains relatively complex and expensive, making them an unattractive choice for operational networks (e.g. Hair et al., 2008).

The Raman technique (section 2.2) permits retrieval of aerosol and cloud vertically-resolved extinction coefficient without any binding assumptions, which are the cornerstone of elastic-based retrieval techniques (section 2.1). Certain instabilities exist, however (Ansmann et al., 1992, Wandinger et al, 1995). In order to reduce the random uncertainty affecting the retrieval, a smoothing of the range-resolved profile is required at expense of the effective vertical resolution (Pappalardo et al., 2004, Iarlori et al., 2015) of the extinction coefficient profile.

Ultimately, different lidar techniques and/or processing algorithms lead to differences of the retrieved vertically-resolved particulate optical properties, affecting the

apparent significance, position and the geometry of observed aerosol and cloud layers. The impact of these differences has never been extensively evaluated. Since lidar-derived optical properties obtained from different instrument techniques are more and more frequently used to assess the direct radiative effects of clouds and aerosols (e.g., Campbell et al., 2016, Lolli et al., 2017a, Tosca et al., 2017), corresponding uncertainties in determining direct radiative effects, which may help reconcile inconsistencies in studies carried out at the global scale based on different lidar techniques, are compulsory, especially now that several new space missions with lidar on board have been launched (Cloud-Aerosol Transport System; CATS, McGill et al., 2015) or are scheduled (European Space Agency Earth Care mission; Illingworth et al., 2015).

The primary goal of this paper is to evaluate the relative differences between the aerosol/cloud direct radiative effects both at surface (SFC) and at the top-of the-atmosphere (TOA) computed using the aerosol/cloud optical properties estimated from more sophisticated versus basic lidar techniques (i.e., Raman vs. elastic lidar). To reach this goal, we use the Fu-Liou-Gu (FLG; Fu and Liou, 1992, Fu and Liou, 1993, Gu et al., 2003, Gu et al., 2011, Lolli et al, 2017b) radiative transfer model to calculate the difference in net direct radiative effect for aerosols and clouds at TOA and SFC for profiles derived from both elastic and combined Raman/elastic lidar techniques.

2. Method

2.1 Elastic and Raman Lidar techniques

Elastic-scattering lidar instruments require assumptions and careful consideration of measurement strategies to constrain the single-scattering lidar equation (Eq. 1), defined as

$$P_r(r) = O(r)K\frac{\beta(r)}{r^2}exp^{-2\int_0^r \alpha(r')dr'} \quad , \quad (1)$$

where $P_r(r)$ is the received power at a range r *and* $O(r)$ is the overlap function, which depends on intersection between the respective telescope and laser field of view. $O(r)$ equals to unity for a distance r_0 depending on the specific lidar system, spanning from few hundred meters to 4-5 km for Micro Pulse Lidar systems (MPL; Campbell et al., 2002). K is the so-called lidar constant (instrument dependent, function of detector quantum and optical efficiencies, telescope diameter, etc.), followed by the two unknown variables, $\beta(r)$ the total backscattering coefficient and $\alpha(r)$ the total extinction coefficient.

A classical method to solving Eq. (1) for single-channel elastic-backscatter lidars (Fernald, 1984) is based on the assumption of the columnar-averaged value of the ratio between the two unknown coefficients, typically indicated by S and called "lidar ratio". The method, due to the large variability of S (i.e., 20-150 sr for aerosols; Ackermann, 1998; Ferrare et al., 2001, Sakai et al., 2003, Müller et al., 2007, Groβ et al., 2011, 2013 and 2015, Veselovskii et al., 2015) translates into large uncertainties associated with the retrieval of α and β (Lolli et al., 2013).

Through greater spectral complexity, it is possible to retrieve α and β with multi-spectral lidars without relying too heavily on fundamental assumptions. For instance, the combined detection of the elastic-backscattered and inelastic backscattered radiation due to the Raman effect by nitrogen (or oxygen) molecules excited to a different vibrational or rotational energy level is possible. Using the Raman lidar technique, we can constrain and rewrite Eq. (1) as

$$\alpha_{\lambda_L}^{par}(r) = \frac{d/dr\left\{\ln\left[n_R(r)/P_r(r)r^2\right]\right\} - \alpha_{\lambda_L}^{mol}(r) - \alpha_{\lambda_R}^{mol}(r)}{1+\left(\lambda_L/\lambda_R\right)^{\text{å}}} \quad (2)$$

where λ_L is the elastic wavelength while λ_R is the wavelength of the Raman scattering, $\alpha_{\lambda_L}^{par}(r)$ represents the particle (aerosols or clouds) extinction coefficient at elastic

wavelength at range *r* while $\alpha_{\lambda_L}^{mol}(r)$ and $\alpha_{\lambda_R}^{mol}(r)$ are the molecular extinction coefficients at wavelengths λ_L and λ_R respectively, $P_r(r)r^2$ is the detected range corrected Raman signal from range *r,* while $n_R(r)$ represents the number density of range-resolved scatters. The wavelength dependence of the particle extinction coefficient is described by the Ångström coefficient, å, defined from the relation

$$\frac{\alpha_{\lambda_L}^{par}(r)}{\alpha_{\lambda_R}^{par}(r)} = \left(\frac{\lambda_R}{\lambda_L}\right)^{å} \quad (3)$$

Eq. (2) allows for independently retrieving vertically-resolved optical coefficients with only very limited *a-priori* assumptions (the Ångström coefficient should be estimated or assumed, but this estimate or assumption, involving a ratio, typically amounts to less than 5% of total error; Ansmann and Müller, 2005). The particle backscattering coefficient, $\beta_{\lambda_R}^{par}(r)$ and $\beta_{\lambda_L}^{par}(r)$, can be derived directly from the ratio of the Raman signal at λ_R and the elastic signal at λ_L.

2.2 Fu-Liou-Gu Radiative Transfer Model

To calculate aerosol and cloud direct radiative effects, we use the one-dimensional FLG radiative transfer model, developed in the early 1990's. The original code has been adapted to retrieve cloud and aerosol direct radiative effects using the aerosol and cloud vertical profile of lidar extinction as input. There exist several parameterizations that provide the vertical profile of cloud microphysics using lidar-retrieved cloud extinction profile, each one with pros and cons, as showed in Comstock et al. (2007). For the purpose of this study and also considering authors past experience (Campbell et al., 2016, Lolli et al., 2017a), we parameterize cirrus clouds through the Heymsfield et al., (2014) empirical relationship conceived expressly for lidar measurements. Here, the cirrus cloud ice crystal average

diameter is directly proportional to the absolute atmospheric temperature (obtained through a radiosonde, regularly launched at measurement site, or numerical reanalysis dataset). Cirrus cloud optical depth and crystal size profiles are used to calculate the single scattering albedo (SSA), phase function and asymmetry factor (AF) at each level.

Similarly, FLG calculates the direct radiative effect of aerosols as a function of the partial contribution of each aerosol species to the total optical depth at each altitude level. FLG uses a lookup table (LUT) with single scattering properties for eighteen different types of aerosols coming from the OPAC (Optical Properties of Aerosol and Clouds) database (d'Almeida et al., 1991; Tegen and Lacis, 1996; Hess et al., 1998). Among all aerosol species, for the initial cases introduced in Section 2.2 we assume that the dust layer is constituted by pure dust advected from Saharan region (aerosol type 17 in FLG), while in the second case we assume pure biomass burning aerosol (aerosol type 11 in FLG). Nevertheless, if the measured aerosol atmospheric profiles do not match exactly the two-selected aerosol types this does not affect the results because we are interested in evaluating the relative discrepancies among the different lidar techniques/data processing. Therefore, what is most relevant in the approach is the application of the same parameterization to each of the different techniques/data processing.

The aerosol/cloud direct radiative effect is calculated subtracting from the FLG total sky run (where aerosols or clouds are present) the FLG run with a pristine atmosphere (control), expressed as

$$DRE = FLG^{TotalSky} - FLG^{Pristine} \quad , \qquad (4)$$

where *DRE* is the direct radiative effect (from aerosols or clouds), while the superscript *TotalSky* means that FLG is computed taking into account the aerosol/cloud profile and *Pristine* represents a hypothetical "clear-sky" atmosphere with no aerosols or clouds.

Direct measurements of aerosol microphysical properties require multi-wavelength lidar (e.g. Veselovskii et al., 2002, 2013), which are not common in many networks and

also are sensitive to systematic and random errors in the optical data (Perez-Ramirez et al., 2013). We focus here on lidar systems that can operate continuously in different networks, and our direct radiative effect calculations do not vary much when changing effective radius and single scattering albedo.

2.3 Direct radiative effect computation

For the analysis in this study, we analyzed lidar data collected with the MUlti-wavelength System for Aerosols (MUSA) Lidar (Madonna et al., 2011), deployed at Consiglio Nazionale delle Ricerche (CNR), Istituto di Metodologie per l'Analisi Ambientale (IMAA) Atmospheric Observatory (CIAO) in Potenza, Italy (40.60N, 15.72E, 760m above sea level; a.s.l). MUSA is a mobile multi-wavelength lidar system based on a Nd:YAG laser source equipped with second and third harmonic generators and on a Cassegrain telescope with a primary mirror of 300mm diameter.

MUSA full angle field-of-view (FOV) and laser beam divergence are large enough (1.0 mrad and 0.6 mrad, respectively) to add important multiple scattering (MS) contributions to the retrieved cirrus extinction coefficient profiles. The Raman extinction coefficient profiles have been corrected for MS as described in Wandinger (1998), taking into account MS contributions by introducing in the respective lidar equation the multiple scattering parameters. These parameters have been calculated, by applying Eloranta's model (Eloranta, 1998) to estimate the contributions of individual orders of multiple scattering. In the model simulations, MUSA specifications (FOV and laser beam divergence) have been used, and a mono-disperse size distribution profile of cirrus cloud ice crystals has been assumed with effective diameters derived from the same parameterization used in FLG model (Heymsfield et al., 2014). The first five scattering orders have been summed.

MUSA lidar system is not tilted due to technical constraints. However, the averaged cirrus cloud retrieved lidar ratios from the combination of Raman and elastic lidar techniques (corrected for MS effects) are 24sr and 26sr, for cirrus cloud cases highlighted here from 10 June 2010 and 17 February 2014, respectively. Those values are consistent with a very low probability of significant specular reflection. The previous statement is supported by the fact that crystal size diameter computed with Heymsfield et al. (2014) parameterization is below 100μm, a threshold value above which the specular reflection can arise. Moreover, in Hogan and Illingworth (2003) work, it is founded that specular reflection tends to be much stronger and more common for temperatures between 250 K and 264 K (that corresponds to much lower altitudes with respect to the examined cirrus cloud cases), where plate crystals, which induce the greatest specular signal, are most common.

The three laser beams at 1064, 532 and 355nm are simultaneously and coaxially transmitted into the atmosphere in a biaxial configuration. The receiving system has three channels for the detection of the radiation elastically backscattered from the atmosphere and two channels for the detection of the Raman radiation backscattered by the atmospheric N_2 molecules at 607 and 387 nm. The elastic channel at 532 nm is split into parallel and perpendicular polarization components by means of a polarizer beamsplitter cube. The backscattered radiation at all the wavelengths is acquired both in analog and photon counting mode. The typical vertical resolution of the raw profiles is 3.75 m with a temporal resolution of 1 min. The system is compact and transportable. It has operated since 2009, and it is one of the reference systems used for the intercomparison of lidar systems within the EARLINET (Pappalardo et al., 2014; Wandinger et al., 2016) Quality Assurance program. In this paper, the data analysis has been carried out considering four observation scenarios at night, as the Raman channel signal shows a much higher signal-to-noise ratio during nighttime:

1) **Dense Dust Aerosol and Biomass Burning Events**. The aerosol extinction profiles are retrieved using the UV (355nm) channel. For each case, the extinction profile is retrieved both with the Raman technique (Ansmann et al., 1990, Whiteman et al., 1992, Veselovskii et al., 2015) and estimated using the sole elastic channel, applying an iterative algorithm (Di Girolamo et al., 1999) with an assigned lidar ratio (S=57 sr for dust case, Mona et al., 2006 and S=63 sr for biomass burning, retrieved averaging the lidar ratio from MUSA Raman channel). Both the Raman and elastic lidar signals have been smoothed by performing a binning of 16 range gates, resulting in a vertical resolution of 60 m. For the Raman channel retrieval, the extinction profile has been calculated using the sliding linear fit technique, with a bin number resulting in an effective vertical resolution of 360 m (Pappalardo et al., 2004). For the elastic channel retrieval, the estimated extinction profile has been first calculated with the signal full vertical resolution of 60 m and then smoothed to the same effective vertical resolution as the Raman extinction profile (360m), using a 2^{nd} order Savitzky-Golay smoothing filter (Press et al., 1992; Iarlori et al., 2015).

2) **Thin and Opaque Cirrus Clouds**. Like aerosols, cirrus cloud extinction profiles are retrieved using the UV (355nm) channel with the Raman technique. The elastic channel retrieval for thin cirrus cloud is obtained applying the same iterative algorithm followed for dust and biomass burning. Although, for the opaque cirrus cloud, due to convergence problems of the iterative method for higher cloud optical depths, we used the MPLNET Level 1.5 cloud product algorithm (Lewis et al., 2016) based on a Klett inversion (Klett, 1985). For both cases (iterative and MPLNET), we assumed a fixed lidar ratio value obtained from Raman and elastic measurements corrected by MS effects of 24sr for thick and 26sr for thin cirrus cloud.

The Raman extinction profile has been calculated with an effective vertical resolution of 420 m (thin cirrus cloud) and 780 m (opaque cirrus cloud), respectively. The iterative (thin cirrus) and MPLNET Level 1.5 cloud algorithm (opaque cirrus; Lewis et al., 2016) extinction profiles are calculated with the original signal vertical resolution of 60 m and smoothed at a resolution of 420 m (thin cirrus) and 780 m (opaque cirrus), respectively, using the Savitzky-Golay filter to match Raman channel spatial resolution.

3) The thermodynamic profile of the atmosphere, needed to calculate the direct radiative effect, is estimated using a standard thermodynamic profile (USS976) mid-latitude model. Emissivity and albedo values are taken from the MODIS Bidirectional Reflectance Distribution Function (BRDF)/Albedo algorithm product (Strahler et al., 1999), with a spatial resolution of 0.1 degrees averaged over a 16-day temporal window (Campbell et al., 2016). As each measured cloud and aerosol extinction profile comes with a relative uncertainty per range bin, the sensitivity of FLG to the input parameters is evaluated applying a Monte Carlo technique. Each extinction profile is replicated 30 times (i.e. a number statistically meaningful), running the MonteCarlo code on the original profile random uncertainty. Likewise, for each replicated extinction profile, the Monte Carlo technique gives a value of surface albedo and profile temperature, based on their respective uncertainties. The direct radiative effect parameters derived for each profile are then represented with a boxplot. It is possible then to quantify the effect of the smoothing calculating the uncertainty from the mean and the standard deviation of the values of net forcing.

3. Results

3.1 Dust and Biomass Burning Event

The analyzed dust event is retrieved from measurements taken on 03 July 2014 at CIAO. Figure 1 shows both the range-corrected composite signal at 1064 nm (Fig. 1a, left panel), and the lidar aerosol extinction profiles at 355 nm (Fig. 1b, left panel) obtained using the Raman technique with an effective resolution of 360 m and estimated using the elastic lidar technique at two different resolutions (60 m and 360 m) and a fixed *S* value obtained analyzing climatological data (S=57sr; Mona et al., 2006). The Raman extinction profile is noisier with respect to those obtained with the iterative method. All profiles, calculated with an integration time of 121 minutes, in the time window from 19:34 UT to 21:40 UT show no significant aerosol loading above 5.5 km.

Figure 3a shows the difference between the estimation of the direct radiative effect using the two considered lidar techniques and data processing at the top-of-the-atmosphere (TOA; Fig 3a, left panel) and surface (SFC; Fig. 3a right panel). The most important contribution to this difference in FLG calculations for this case is related to the adopted lidar technique (red arrows in Fig. 3a, left and right panels) and not to the effective vertical resolution determined by the smoothing (blue arrows in Fig. 3a, left and right panels). This characteristic is invariant switching from TOA (Fig. 3a right panel) to SFC (Fig. 3a left panel) and is mainly the result of the assumption of a fixed lidar ratio to estimate the aerosol extinction profile using the elastic technique.

For the dust case, the net direct radiative effect determined with the two different lidar techniques differs by 0.7 W/m^2 (5%) at SFC and 0.85 W/m^2 (6%) at TOA. In absolute magnitudes, these net total forcing values are larger than the uncertainty, on average, estimated direct effect by IPCC (mean -0.5 W/m^2, range -0.9 to -0.1). The contribution due to smoothing is negligible in comparison.

The analyzed biomass burning case study is retrieved from measurements taken on 19 June 2013 at CIAO integrating the signal temporally from 19:27 UT to 20:48 UT. The extinction profiles used as input into the FLG radiative transfer model were retrieved in the

same way as for the dust case. Instead of a climatological lidar ratio value at 355nm, however, we used S=63 sr, obtained by averaging the lidar ratio profile retrieved with combined Raman-elastic techniques in the biomass burning layer. In Figure 1b (right panel) are the extinction profiles obtained from both the Raman and iterative methods (full resolution and smoothed over 360m window). Figure 3b shows the difference in biomass burning direct radiative effects with respect to the different lidar and data processing techniques. Similar to the dust case event, the bigger differences are found to be related to the different lidar techniques both at SFC (0.05 W/m^2 or 5%; red arrows, Fig. 3b right panel) and at TOA (0.007 W/m^2 or 5%; Fig. 3b left panel).

The analysis shows how the mixing of different lidar techniques in a specific study or in the routine operations of an aerosol network at regional or global scale must take into account of the uncertainties related to the assumptions that are behind the retrieval of the optical properties. This is important not only to provide a complete assessment of the total uncertainty budget for each lidar product, but also to enable a physically consistent use of the lidar data in the estimation of the direct radiative effect and, likely, for many other user-oriented applications based on lidar data.

3.2 Cirrus cloud

Similar to Fig.1, Figs. 2a and 2b shows the composite range-corrected signal and three extinction profiles retrieved from Raman lidar measurements of cirrus clouds with a vertical resolution of 420 m (thin cirrus, Fig 2a,b left panel) and 780 m (opaque cirrus, Fig 2a,b right panel), and with the elastic channel at two vertical resolutions (60m and 420m iterative method for thin cirrus cloud; 60m and 780 m MPLNET Level 1.5 cloud product algorithm for opaque cirrus cloud) using a MS corrected lidar ratio of 24sr (opaque cirrus) and 26sr (thin cirrus) . The obtained cloud extinction profiles from the different lidar and data processing techniques are averaged over 42 minutes, in the time window from 01:29

354 UT to 02:13 UT on 17 February 2014 (thin cirrus) and from 19:40 UT to 20:44 UT on 10
355 June 2010 (opaque cirrus), respectively.

356 Figure 4a depicts the results obtained for cirrus cloud measurements taken on 17
357 February 2014. Here we have a completely different situation with respect to the aerosol
358 cases. That is, the discrepancies between the Raman and elastic lidar techniques (red arrows
359 in Fig. 4a, left and right panels) are much smaller than the discrepancies due to the effective
360 vertical resolution of the extinction coefficient profile both at TOA and SFC (blue arrows
361 in Fig. 4a, left and right panels). This is related to what is typically a much stronger
362 extinction coefficient for clouds than for aerosols. In this cirrus cloud case, the direct
363 radiative effect determined with the two different lidar techniques differs by about 1.2
364 W/m^2 (16%) at TOA and 0.04 W/m^2 (4%) at SFC, while the effect of smoothing within a
365 window of 420 m provides an additional difference of 2.7 W/m^2 (47%) at TOA and about
366 0.55 W/m^2 (53%) at SFC.

367 Results from the opaque cirrus cloud (Fig. 4b, left and right panels) exhibit a similar
368 behavior to the thin cirrus cloud, with signal smoothing outweighing the impact of the lidar
369 technique (blue arrow). The order of magnitude is similar to the thin cirrus cloud, with a
370 difference at TOA between techniques of 4.6 W/m^2 (14%) and 1.6 W/m^2 (11%) at SFC. In
371 contrast, the difference in data processing is of 11.8 W/m^2 (39%) at TOA and 7.7 W/m^2
372 (64%) at SFC. The results are evidence of the critical need to study cirrus clouds using
373 high-resolution profiles of the optical properties to provide an accurate estimation of the
374 cloud direct radiative effect.

375

376 ***4. Conclusions and future perspectives***

377 We applied the adapted Fu-Liou-Gu (FLG) radiative transfer model to quantitatively
378 evaluate how much the lidar and/or data processing technique applied influence the net
379 direct radiative effect exerted by two different upper atmospheric aerosol layers (dust and

biomass burning) and a thin versus opaque cirrus cloud layer, both at top-of-the-atmosphere (TOA) and surface (SFC). The evaluation has been made using aerosol/cloud extinction atmospheric profiles as inputs into FLG radiative transfer model retrieved using the Raman/elastic technique and as estimated by lidar elastic measurements only (iterative method for aerosol layers and thin cirrus cloud; NASA Micro-Pulse Lidar Network Level 1.5 cloud algorithm for opaque cirrus cloud). Because the Raman measurement retrieval is unstable due to the derivative of the signal at the numerator (see Eq. 2), a smoothing of the range-corrected signal is necessary to reduce the associated random uncertainty. The same processing treatment has been applied also to the elastic measurement signals.

The results show that the difference in direct radiative effect between the lidar and data processing/smoothing techniques applied is mostly unvaried at TOA and SFC. For the dust and biomass burning episodes, the data processing/smoothing does not play a major role, but instead the lidar measurement technique is more important with respect to the final result. This can be explained by the large variability of the lidar ratio (i.e., the unknown extinction-to-backscatter ratio used to constrain the single-solution lidar equation) compared to the assumed value. The opposite is true for cirrus clouds, where the applied data processing/smoothing play a fundamental role in determining sensitivities in the final results. This is due to the smoothing effect on the observed sharp structures that strongly alters the vertical structure and the extinction of the cloud.

Summarizing, we found that for the aerosol cases, the main difference both at TOA and SFC is driven by the respective lidar technique and not the data processing, with a difference on dust direct radiative effect of 0.7 W/m^2 (5%) at SFC and 0.85 W/m^2 (6%) at TOA. Similarly, for biomass burning we found a discrepancy 0.05 W/m^2 (5%) at SFC and 0.007 W/m^2 (5%) at TOA. For the cirrus clouds, the data smoothing is producing larger differences with respect to the lidar technique. On the contrary, using a different data processing/smoothing implies a larger difference in cirrus cloud direct radiative effect. A

discrepancy of 0.55 W/m^2 (53%) is found at SFC while about 2.7 W/m^2 (47%) at TOA for the thin cirrus cloud. Similarly for the opaque cirrus, the discrepancies produced by data processing/smoothing are larger with respect to the different lidar technique. At SFC we find a difference of 7.7 W/m^2 (64%) and 11.8 W/m^2 at TOA (39%).

A possible explanation of this different behavior is that the FLG radiative transfer model calculations are strongly dependent on the optical depth of the examined atmospheric layer. At coarse resolution (cloud) the smoothing is producing changes in the extinction profile that translates into creation/suppression of ice crystals that have a strong influence on direct radiative effect. At finer resolution, as in the case of aerosol case studies, the smoothing is just producing fluctuations that do not influence the total radiative effect. In this case, the lidar technique is making a big difference, as an assumed wrong value for lidar ratio (*S*) that has a much larger variability with respect to the clouds, will amplify or suppress the aerosol peak that will translate into a higher/lower radiative effect.

With this study, we wish to draw attention in speculating how much the derived aerosol and cloud radiative effect is dependent on the lidar measurement and retrieval techniques, as well as on the data processing constraints/assumptions. This dependence looks increasingly relevant for existing and future space missions involving lidar instrument, as well as for the GAW Atmospheric LIdar Observation Network (GALION; Hoff et al., 2008) project, which features then main objective of federating all existing ground-based lidar networks to provide atmospheric measurement profiles of the aerosol and cloud optical and microphysical properties with sufficient coverage, accuracy and resolution. For future work, it is imperative on the community to continue understanding and refining what are the limits of the each lidar technique along with the related retrieval algorithms adopted in each ground-based network. FLG or any other well-established radiative transfer model then can be used as diagnostic tool to assure data quality through continued

intercomparisons with real observation both at ground (using flux measurements), in situ (aircraft measurements) and at TOA (using satellite-based measurements).

References

Ackermann J., (1998): The Extinction-to-Backscatter Ratio of Tropospheric Aerosol: A Numerical Study. *J. Atmos. Oceanic Technol.*, **15**, 1043–1050.

Ansmann, A., M. Riebesell, and C. Weitkamp, (1990): Measurement of atmospheric aerosol extinction profiles with a Raman lidar. *Opt. Lett*, **15,** 746–748

Ansmann, A., Wandinger, U., Riebesell, M., Weitkamp, C., Michaelis, W., (1992)," Independent measurement of extinction and backscatter profiles in cirrus clouds by using a combined raman elastic-backscatter lidar", Applied Optics, 31 (33), pp. 7113-7131

Ansmann, A. and Müller, D., (2005), "Lidar and atmospheric aerosol particles", in: *LIDAR – Range–resolved optical remote sensing of the atmosphere*, edited by: Weitkamp, C., Springer, New York, USA, 105–141

Antuña-Marrero, J.C., E. Landulfo, R. Estevan, B. Barja, A. Robock, E. Wolfram, P. Ristori, B. Clemesha, F. Zaratti, R. Forno, E. Armandillo, Á.E. Bastidas, Á.M. de Frutos Baraja, D.N. Whiteman, E. Quel, H.M. Barbosa, F. Lopes, E. Montilla-Rosero, and J.L. Guerrero-Rascado, (2015): LALINET: The first Latin American-born regional atmospheric observational network. *Bull. Amer. Meteor. Soc.,* **0**, doi: 10.1175/BAMS-D-15-00228.1.

Asmi, A., Collaud Coen, M., Ogren, J. A., Andrews, E., Sheridan, P., Jefferson, A., ... & Kivekäs, N. (2013). Aerosol decadal trends–Part 2: In-situ aerosol particle number concentrations at GAW and ACTRIS stations. *Atmospheric Chemistry and Physics*, *13*(2), 895-916.

456 Bösenberg, J and R Hoff, (2008), GAW Aerosol Lidar Observation Network (GALION),
457 WMO GAW Report (WMO, Geneva, Switzerland)
458 Campbell, J. R., D. L. Hlavka, E. J. Welton, C. J. Flynn, D. D. Turner, J. D. Spinhirne, V.
459 S. Scott III, and I. H. Hwang, (2002). "Full-time, eye-safe cloud and aerosol lidar
460 observation at atmospheric radiation measurement program sites: Instruments and
461 data processing." *Journal of Atmospheric and Oceanic Technology* 19, no. 4: 431-
462 Campbell, J.R., S. Lolli, J.R. Lewis, Y. Gu, and E.J. Welton, (2016), "Daytime Cirrus
463 Cloud Top-of-the-Atmosphere Radiative Forcing Properties at a Midlatitude Site
464 and Their Global Consequences", *Journal of Applied Meteorology and*
465 *Climatology, 55*, 8, 1667-1679
466 Comstock, J. M., S. A. McFarlane, R. d'Entremont, D. DeSlover, D.D. Turner, G.G. Mace,
467 S.Y. Matrosov, M.D. Shupe, P. Minnis, D. Mitchell, K. Sassen, and Z.
468 Wang, (2007):An Intercomparison of Microphysical Retrieval Algorithms for
469 Upper-Tropospheric Ice Clouds. *Bull. Amer. Meteor. Soc.,* **88**, 191–
470 204, https://doi.org/10.1175/BAMS-88-2-191
471 d'Almeida, G. A., Koepke, P., and Shettle, E. P. (1991): Atmospheric aerosols – global
472 climatology and radiative characteristics, A. Deepak Publishing, Hampton,
473 Virginia, 561 pp.
474 Di Girolamo, P., P. F. Ambrico, A. Amodeo, A. Boselli, G. Pappalardo, and N. Spinelli
475 (1999), Aerosol observations by lidar in the nocturnal boundary layer, Appl. Opt.,
476 38 (21), 4585–4595.
477 Illingworth, A. J., Hogan, R. J., O'connor, E. J., Bouniol, D., Delanoë, J., Pelon, J., ... &
478 Donovan, D. P. (2007). Cloudnet: Continuous evaluation of cloud profiles in seven
479 operational models using ground-based observations. *Bulletin of the American*
480 *Meteorological Society*, *88*(6), 883-898.

Diner, D.J., Beckert, J.C., Reilly, T.H., Bruegge, C.J., Conel, J.E., Kahn, R.A., Martonchik, J.V., Ackerman, T.P., Davies, R., Gerstl, S.A.W., Gordon, H.R., Muller, J.-P., Myneni, R.B., Sellers, P.J., Pinty, B., Verstraete, M.M. Multi-angle imaging spectroradiometer (MISR) instrument description and experiment overview (1998) IEEE Transactions on Geoscience and Remote Sensing, 36 (4), pp. 1072-1087

Di Girolamo, L., T. C. Bond, D. Bramer, D. J. Diner, F. Fettinger, R. A. Kahn, J. V. Martonchik, M. V. Ramana, V. Ramanathan, and P. J. Rasch. (2004). "Analysis of Multi- angle Imaging SpectroRadiometer (MISR) aerosol optical depths over greater India during winter 2001–2004." *Geophysical Research Letters* 31, no. 23

Dubovik, O., Smirnov, A., Holben, B. N., King, M. D., Kaufman, Y. J., Eck, T. F., & Slutsker, I. (2000). Accuracy assessments of aerosol optical properties retrieved from Aerosol Robotic Network (AERONET) Sun and sky radiance measurements. *Journal of Geophysical Research: Atmospheres*, *105*(D8), 9791-9806.

Eck, T. F., Holben, B. N., Reid, J. S., Arola, A., Ferrare, R. A., Hostetler, C. A., ... & Lyapustin, A. (2014). Observations of rapid aerosol optical depth enhancements in the vicinity of polluted cumulus clouds. *Atmospheric Chemistry and Physics*, *14*(21), 11633.

Eloranta, E.E., "Practical model for the calculation of multiply scattered lidar returns", Applied Optics, Vol.37, N.12, 2464 – 2472, 1998

Ferrare, R. A., D. D. Turner, L. H. Brasseur, W. F. Feltz, O. Dubovik, and T. P. Tooman(2001), Raman lidar measurements of the aerosol extinction-to-backscatter ratio over the Southern Great Plains, J. Geophys. Res., 106(D17), 20333–20347

Ferrare, R., Feingold, G., Ghan, S., Ogren, J., Schmid, B., Schwartz, S.E. and Sheridan, P., 2006. Preface to special section: Atmospheric Radiation Measurement Program

May 2003 Intensive Operations Period examining aerosol properties and radiative influences. *Journal of Geophysical Research: Atmospheres*, *111*(D5).

Fu Q, Liou K.N., (1992): On the correlated k-distribution method for radiative transferin nonhomogeneous atmospheres. J. Atmos. Sci. 49:2139 2156.

Fu Q, Liou K.N., (1993): Parametrization of the radiative properties of cirrus clouds. J. Atmos. Sci. 50:2008-2025.

Goldsmith, J. E. M., F. H. Blair, S. E. Bisson, and D. D. Turner, (1998): Turn-Key Raman lidar for profiling atmospheric water vapor, clouds, and aerosols. *Appl. Opt.,* **37,** 4979–4990.

Groß, S. M. Tesche, V. Freudenthaler, Ca. Toledano, M. Wiegner, A. Ansmann, D. Althausen and M. Seefeldner (2011) Characterization of Saharan dust, marine aerosols and mixtures of biomass-burning aerosols and dust by means of multi-wavelength depolarization and Raman lidar measurements during SAMUM 2, Tellus B: Chemical and Physical Meteorology, 63:4, 706-724

Groß, S., Esselborn, M., Weinzierl, B., Wirth, M., Fix, A., and Petzold, A. (2013): Aerosol classification by airborne high spectral resolution lidar observations, Atmos. Chem. Phys., 13, 2487-2505, https://doi.org/10.5194/acp-13-2487-2013.

Groß, S., Freudenthaler, V., Schepanski, K., Toledano, C., Schäfler, A., Ansmann, A., and Weinzierl, B. (2015): Optical properties of long-range transported Saharan dust over Barbados as measured by dual-wavelength depolarization Raman lidar measurements, Atmos. Chem. Phys., 15, 11067-11080

Grund, C. J. and E. W.Eloranta, (1991), "University of Wisconsin High Spectral Resolution Lidar," *Optical Engineering*, **30**, 6--12, 1991.

Gu Y, Farrara J, Liou KN, Mechoso C. R., (2003): Parametrization of cloud-radiativeprocesses in the UCLA general circulation model. *J. Climate* 16:3357-3370.

Gu Y, Liou KN, Ou SC, Fovell R, (2011): Cirrus cloud simulations using WRF withimproved radiation parametrization and increased vertical resolution. *J. Geophys. Res*.116:D06119.

Hair, J. W., Hostetler, C. A., Cook, A. L., Harper, D. B., Ferrare, R. A., Mack, T. L., Welch, W., Izquierdo, L. R., and Hovis, F. E. (2008): Airborne High Spectral Resolution Lidar for profiling aerosol optical properties, Appl. Optics, 47, 6734–6752, 2008.

Hess, M., Koepke, P., and Schult, I. (1998): Optical properties of aerosols and clouds: The software package OPAC, B. *Am. Meteorol. Soc*., 79, 831–844.

Heymsfield, A., D. Winker, M. Avery, M. Vaughan, G. Diskin, M. Deng, V. Mitev, and R. Matthey, (2014): Relationships between ice water content and volume extinction coefficient from in situ observations for temperatures from 0° to −86°C: Implications for spacebornelidar retrievals. *J. Appl. Meteor. Climatol*., 53, 479–505

Hoff, R. M., Bösenberg, J., & Pappalardo, G. (2008, June). The GAW Aerosol Lidar Observation Network (GALION). In Reviewed and Revised Papers Presented at the 24th International Laser Radar Conference (pp. 23-27).

Iarlori, M., Madonna, F., Rizi, V., Trickl, T., and Amodeo, A., (2015): Effective resolution concepts for lidar observations, Atmos. Meas. Tech., 8, 5157-5176, doi:10.5194/amt-8-5157-2015.

Illingworth, A.J., Barker, H.W., Beljaars, A., Ceccaldi, M., Chepfer, H., Clerbaux, N., Cole, J., Delanoë, J., Domenech, C., Donovan, D.P., Fukuda, S., Hirakata, M., Hogan, R.J., Huenerbein, A., Kollias, P., Kubota, T., Nakajima, T., Nakajima, T.Y., Nishizawa, T., Ohno, Y., Okamoto, H., Oki, R., Sato, K., Satoh, M., Shephard, M.W., Velázquez-Blázquez, A., Wandinger, U., Wehr, T., Van Zadelhoff, G.-J.(2015) The earthcare satellite: The next step forward in global measurements of clouds, aerosols, precipitation, and radiation Bulletin of the American Meteorological Society, 96 (8), pp. 1311-1332

559 IPCC, 2012: Managing the Risks of Extreme Events and Disasters to Advance Climate
560 Change Adaptation. A Special Report of Working Groups I and II of the
561 Intergovernmental Panel on Climate Change [Field, C.B., V. Barros, T.F. Stocker,
562 D. Qin, D.J. Dokken, K.L. Ebi, M.D. Mastrandrea, K.J. Mach, G.-K. Plattner, S.K.
563 Allen, M. Tignor, and P.M. Midgley (eds.)]. Cambridge University Press,
564 Cambridge, UK, and New York, NY, USA, 582 pp.
565 IPCC, 2014: Climate Change, (2014): Impacts, Adaptation, and Vulnerability. Part A:
566 Global and Sectoral Aspects. Contribution of Working Group II to the Fifth
567 Assessment Report of the Intergovernmental Panel on Climate Change [Field, C.B.,
568 V.R. Barros, D.J. Dokken, K.J. Mach, M.D. Mastrandrea, T.E. Bilir, M. Chatterjee,
569 K.L. Ebi, Y.O. Estrada, R.C. Genova, B. Girma, E.S. Kissel, A.N. Levy, S.
570 MacCracken, P.R. Mastrandrea, and L.L. White (eds.)]. *Cambridge University*
571 *Press, Cambridge, United Kingdom and New York, NY, USA*, 1132 pp.
572 Kahn, R. A., David L. Nelson, Michael J. Garay, Robert C. Levy, Michael A. Bull, David
573 J. Diner, John V. Martonchik, Susan R. Paradise, Earl G. Hansen, and Lorraine A.
574 Remer. "MISR aerosol product attributes and statistical comparisons with
575 MODIS." *IEEE Transactions on Geoscience and Remote Sensing*47, no. 12 (2009):
576 4095-4114
577 Khor W. Y, Matjafri M. Z., Lim H.; Hee W. S ; Lolli S., (2015): One-year monitoring of
578 the atmosphere over Penang Island using a ground-based lidar *Proc. SPIE 9645,*
579 *Lidar Technologies, Techniques, and Measurements for Atmospheric Remote*
580 *Sensing* XI, 96450M (October 20, 2015); doi:10.1117/12.2195440.
581 King, Michael D., W. Paul Menzel, Yoram J. Kaufman, Didier Tanré, Bo-Cai Gao, Steven
582 Platnick, Steven A. Ackerman, Lorraine A. Remer, Robert Pincus, and Paul A.
583 Hubanks, (2003), "Cloud and aerosol properties, precipitable water, and profiles of

temperature and water vapor from MODIS." *IEEE Transactions on Geoscience and Remote Sensing* 41, no. 2: 442-458.

J. Klett, (1985), "Lidar inversion with variable backscatter/extinction ratios," Appl. Opt. 24, 1638-1643.

Lewis, J. R., J. R. Campbell, E. J. Welton, S. A. Stewart, and P. C. Haftings, (2016): Overview of MPLNET, version 3, cloud detection. J. Atmos. Oceanic Technol., 33 , 2113–2134, doi: 10.1175/JTECH-D-15-0190.1

Lolli S. et al, (2013), "Evaluating light rain drop size estimates from multiwavelength micropulse lidar network profiling.,"*J. Atmos. Oceanic Technol.*, **30**, 2798–2807.

Lolli S. ; E. J. Welton ; A. Benedetti ; L. Jones ; M. Suttie ; S-H. Wang, (2014)." MPLNET lidar data assimilation in the ECMWF MACC-II Aerosol system: evaluation of model performances at NCU lidar station." *Proc. SPIE 9246, Lidar Technologies, Techniques, and Measurements for Atmospheric Remote Sensing* X, 92460I (October 20, 2014); doi:10.1117/12.2068201

Lolli S., Di Girolamo, P. (2015)." Principal component analysis approach to evaluate instrument performances in developing a cost-effective reliable instrument network for atmospheric measurements." Journal of Atmospheric and Oceanic Technology, Vol. 32 (9), 1642-1649.

Lolli, S., J.R. Campbell, J.R. Lewis, Y. Gu, J.W. Marquis, B.N. Chew, S. Liew, S.V. Salinas, and E.J. Welton, (2017a): Daytime Top-of-the-Atmosphere Cirrus Cloud Radiative Forcing Properties at Singapore. *J. Appl. Meteor. Climatol.,* **56**, 1249–1257, doi: 10.1175/JAMC-D-16-0262.1.

Lolli, S., Campbell, J. R., Lewis, J. R., Gu, Y., and Welton, E. J. (2017b): Technical note: Fu–Liou–Gu and Corti–Peter model performance evaluation for radiative retrievals from cirrus clouds, Atmos. Chem. Phys., 17, 7025-7034, https://doi.org/10.5194/acp-17-7025-2017.

Madonna, F., Amodeo, A., Boselli, A., Cornacchia, C., Cuomo, V., D'Amico, G., Giunta, A., Mona, L., and Pappalardo, G. (2011): CIAO: the CNR-IMAA advanced observatory for atmospheric research, *Atmos. Meas. Tech*., 4, 1191-1208, doi:10.5194/amt-4-1191-2011.

Madonna, F., A. Amodeo, G. D'Amico, and G. Pappalardo (2013), A study on the use of radar and lidar for characterizing ultragiant aerosol, Journal of Geophys. Res., DOI: 10.1002/jgrd.50789.

Madonna F., A. Amodeo, G. D'Amico, L. Mona, and G. Pappalardo (2010), Observation of non-spherical ultragiant aerosol using a microwave radar, Geophys. Res. Lett., 37, L21814, doi:10.1029/2010GL044999.

McComiskey, A. and R.A. Ferrare, 2016: Aerosol Physical and Optical Properties and Processes in the ARM Program. *Meteorological Monographs,* **57**, 21.1–21.17,

McGill, M.J., Yorks, J.E., Scott, V.S., Kupchock, A.W., Selmer, P.A. The Cloud-Aerosol Transport System (CATS): A technology demonstration on the International Space Station (2015) *Proceedings of SPIE - The International Society for Optical Engineering,* 9612, art. no. 96120A

Mona, L., Amodeo, A., Pandolfi, M., & Pappalardo, G,. (2006). Saharan dust intrusions in the Mediterranean area: Three years of Raman lidar measurements. *Journal of Geophysical Research: Atmospheres*, *111*(D16).

Mona, L., Amodeo, A., D'Amico, G., Giunta, A., Madonna, F., & Pappalardo, G. (2012). Multi-wavelength Raman lidar observations of the Eyjafjallajökull volcanic cloud over Potenza, southern Italy. *Atmospheric Chemistry and Physics*, *12*(4), 2229-2244.

Müller, D., A. Ansmann, I. Mattis, M. Tesche, U. Wandinger, D. Althausen, and G. Pisani(2007), Aerosol-type-dependent lidar ratios observed with Raman lidar, J. Geophys. Res., 112, D16202.

Pappalardo, G., Amodeo, A., Mona, L., Pandolfi, M., Pergola, N., & Cuomo, V. (2004). Raman lidar observations of aerosol emitted during the 2002 Etna eruption. *Geophysical Research Letters*, *31*(5).

Pappalardo, G., Amodeo, A., Apituley, A., Comeron, A., Freudenthaler, V., Linné, H., Ansmann, A., Bösenberg, J., D'Amico, G., Mattis, I., Mona, L., Wandinger, U., Amiridis, V., Alados-Arboledas, L., Nicolae, D., and Wiegner, M, (2014). EARLINET: towards an advanced sustainable European aerosol lidar network, *Atmos. Meas. Tech*., 7, 2389-2409, doi:10.5194/amt-7-2389-2014,

Pappalardo G., A. Amodeo, M. Pandolfi, U. Wandinger, A. Ansmann, J. Bosenberg, V. Matthias, V. Amiridis, F. De Tomasi, M. Frioud, M. Iarlori, L. Komguem, A. Papayannis, F. Rocadenbosch, and X. Wang, (2004) "Aerosol lidar intercomparison in the framework of the EARLINET, project. 3. Raman lidar algorithm for aerosol extinction, backscatter and lidar ratio", *Appl. Opt.,* 43(28), 5370–5385.

Pérez-Ramírez, D., Whiteman, D.N., Veselovskii, I., Kolgotin, A., Korenskiy, M., Alados-Arboledas, L. (2013) Effects of systematic and random errors on the retrieval of particle microphysical properties from multiwavelength lidar measurements using inversion with regularization. Atmospheric Measurement Techniques 6, 3039-3054.

Perez-Ramirez, D., Lyamani, H., Olmo, F.J., Whiteman, D.N., and Alados-Arboledas, L. (2012) Columnar aerosol properties from sun-and-star photometry: statiscal comparisons and day-to-night dynamic. Atmospheric Chemistry and Physics, 12, 9719-9738**.**

Press, W.H., B. P. Flannery, S. A. Teukolsky, and W. T. Vetterling, 1992 "Numerical Recipes in FORTRAN: The Art of Scientific Computing", *2nd ed., Cambridge, U. Press, Cambridge*, pp. 127–128 and 644–647.

662 Remer, L.A., Kaufman, Y.J., Tanré, D., Mattoo, S., Chu, D.A., Martins, J.V., Li, R.-R.,
663 Ichoku, C., Levy, R.C., Kleidman, R.G., Eck, T.F., Vermote, E., Holben, B.N. The
664 MODIS aerosol algorithm, products, and validation 2005, *Journal of Atmospheric*
665 *Sciences,* 62 (4), pp. 947-973
666 Sakai, T., T. Shibata, K. Hara, M. Kido, K. Osada, M. Hayashi, K. Matsunaga, and Y.
667 Iwasaka(2003), Raman lidar and aircraft measurements of tropospheric aerosol
668 particles during the Asian dust event over central Japan: Case study on 23 April
669 1996, J. Geophys. Res., 108, 4349
670 Shipley, S. T., Tracy, D. H., Eloranta, E. W., Trauger, J. T., Sroga, J. T., Roesler, F. L.,
671 and Weinman, J. A., (1983): High Spectral Resolution Lidar to Measure Optical-
672 Scattering Properties of Atmospheric Aerosols, 1. Theory and Instrumentation,
673 Appl. Optics, 22, 3716–3724.
674 Strahler, A. H., C. B. Schaaf, J.-P. Muller, W. Warmer, M. J. Barnsley, R. d'Entremont, B.
675 Hu, P. Lewis, X. Li, and E. V. Ruiz de Lope, 1999: MODIS BRDF/albedo product:
676 Algorithm theoretical basis document. *NASA EOS-MODIS Doc*. ATBD-MOD-09,
677 version 5.0
678 Sugimoto, N., Matsui, I., Shimizu, A., Nishizawa, T., Hara, Y., Uno, I. Lidar network
679 observation of tropospheric aerosols (2010) *Proceedings of SPIE - The*
680 *International Society for Optical Engineering, 7860*, art. no. 78600J
681 Smirnov, A., Holben, B. N., Eck, T. F., Slutsker, I., Chatenet, B., & Pinker, R. T. (2002).
682 Diurnal variability of aerosol optical depth observed at AERONET (Aerosol
683 Robotic Network) sites. *Geophysical Research Letters*, *29*(23).
684 Tanré, D., Y. J. Kaufman, M. Herman, and S. Mattoo. "Remote sensing of aerosol
685 properties over oceans using the MODIS/EOS spectral radiances." *Journal of*
686 *Geophysical Research: Atmospheres* 102, no. D14 (1997): 16971-16988.

687 Tanré, D., F. M. Bréon, J. L. Deuzé, O. Dubovik, F. Ducos, P. François, P. Goloub, M.
688 Herman, A. Lifermann, and F. Waquet. "Remote sensing of aerosols by using
689 polarized, directional and spectral measurements within the A-Train: the
690 PARASOL mission." *Atmospheric Measurement Techniques* 4, no. 7 (2011): 1383-
691 1395.
692 Tegen, I. and Lacis, A. A.: Modeling of particle size distribution and its influence on the
693 radiative properties of mineral dust aerosol (1996), *J. Geophys. Res*., 101, 19237–
694 19244, 1996.
695 Tosca, M. G., Campbell, J., Garay, M., Lolli, S., Seidel, F. C., Marquis, J., & Kalashnikova,
696 O. (2017). Attributing accelerated summertime warming in the southeast united
697 states to recent reductions in aerosol burden: Indications from vertically-resolved
698 observations. *Remote Sensing*, *9*(7), 674.
699 Veselovskii, I., Kolgotin, A., Griaznov, V., Muller, D., Wandinger, U., Whiteman, D.
700 (2002) Inversion with regularization for the retrieval of tropospheric aerosol
701 parameters from multiwavelength lidar sounding. Applied Optics 41, 3685-3699.
702
703 Veselovskii, I., Whiteman, D.N., Korenskiy, M., Kolgotin, A. Dubovik, O., Pérez-
704 Ramírez, D., Suvorina, A,. (2013) Retrieval of spatio-temporal distributions of
705 particle parameters from multiwavelength lidar measurements using the linear
706 estimation technique and comparison with AERONET. Atmospheric Measurement
707 Techniques, 6, 2671-2682
708 Veselovskii, I., Whiteman, D.N., Korenskiy, M., Suvorina, A., Pérez-Ramírez, D., (2015)
709 Use of rotational Raman measurements in multiwavelength aerosol lidar for
710 evaluation of particle backscattering and extinction. Atmospheric Measurement
711 Techniques 8, 4111-4122.

712 Wandinger, U., Ansmann, A., Reichardt, J., Deshler, T. Determination of stratospheric
713 aerosol microphysical properties from independent extinction and backscattering
714 measurements with a Raman lidar (1995) *Applied Optics*, 34 (36), pp. 8315-8329.
715 Wandinger,U., (1998) "Multiple-scattering influence on extinction and backscatter
716 coefficient measurements with Raman and high-spectral resolution lidars", Applied
717 Optics, Vol.37, N.3, 417 – 427.
718 Wandinger, U., Freudenthaler, V., Baars, H., Amodeo, A., Engelmann, R., Mattis, I.,
719 Gross., S., Pappalardo, G., Giunta, A., D'Amico, G., Chaikovsky, A., Osipenko, F.,
720 Slesar, A., Nicolae, D., Belegante, L., Talianu, C., Serikov, I., Linn., 491 H., Jansen,
721 F., Apituley, A., Wilson, K. M., de Graaf, M., Trickl, T., Giehl, H., Adam, M.,
722 Comer.n, A., Mu.oz-Porcar, C., Rocadenbosch, F., Sicard, M., Tom.s, S., Lange,
723 D., Kumar, D., Pujadas, M., Molero, F., Fern.ndez, A. J., Alados-Arboledas, L.,
724 Bravo-Aranda, J. A., Navas-Guzm.n, F., Guerrero-Rascado, J. L., Granados-
725 Munoz, M. J., Prei.ler, J., Wagner, F., Gausa, M., Grigorov, I., Stoyanov, D., Iarlori,
726 M., Rizi, V., Spinelli, N., Boselli, A., Wang, X., Lo Feudo, T., Perrone, M. R., De
727 Tomasi, F., and Burlizzi, P., 2016: EARLINET instrument intercomparison
728 campaigns: overview on strategy and results, Atmos. Meas. Tech., 9, 1001-1023,
729 doi:10.5194/amt-9-1001-2016
730 Whiteman, D. N., Melfi, S. H., & Ferrare, R. A. (1992). Raman lidar system for the
731 measurement of water vapor and aerosols in the Earth's atmosphere. *Applied*
732 *Optics*, *31*(16), 3068-3082.
733 Whiteman, D.N. Examination of the traditional Raman lidar technique. II. Evaluating the
734 ratios for water vapor and aerosols (2003) *Applied Optics*, 42 (15), pp. 2593-2608
735 Whiteman, D.N., Pérez-Ramírez, D., Veselovskii, I., Colarco, P., Buchard, V. (2018)
736 Simulations of spaceborne multiwavelength lidar measurements and retrievals of

737 aerosol microphysics. Journal of Quantitative Spectroscopy and Radiative Transfer,
738 Volume 205, 2018, Pages 27-39.
739 Winker, D. M., W. H. Hunt, and M. J. McGill (2007), Initial performance assessment of
740 CALIOP, Geophys. Res. Lett., 34, L19803, doi:10.1029/2007GL030135.
741 Welton, E. J., Voss, K. J., Quinn, P. K., Flatau, P. J., Markowicz, K., Campbell, J. R.,
742 Johnson, J. E. (2002). Measurements of aerosol vertical profiles and optical
743 properties during INDOEX 1999 using micropulse lidars. *Journal of Geophysical*
744 *Research: Atmospheres*, *107*(D19).
745

Figures

a)

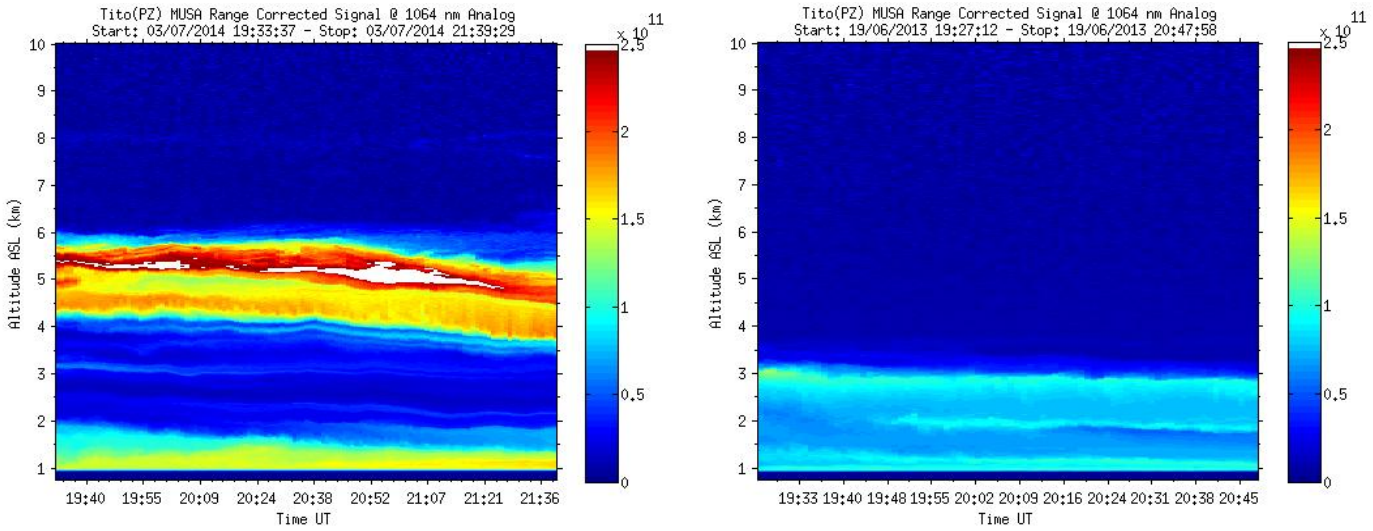

b)

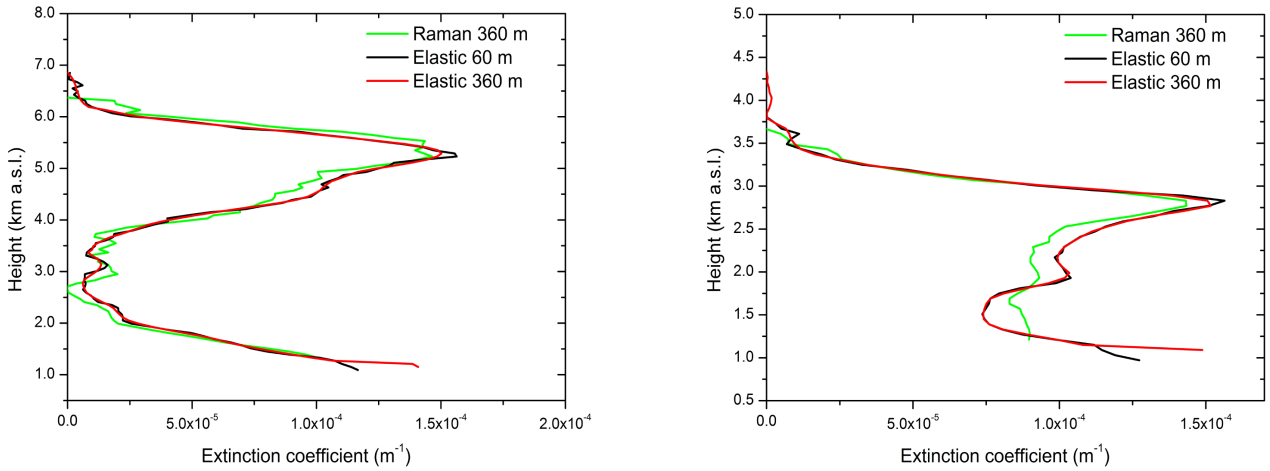

Figure 1 a): composite plot of the range corrected signal at 1064nm showing a well-defined dust layer at about 5 km a.s.l. (left panel) and for a biomass burning aerosol layer at about 2 km (right panel). b): aerosol lidar extinction profiles at 355nm retrieved with the Raman and the elastic lidar techniques with different spatial resolutions (60m and 360m) for dust (signal temporally integrated from 19:34UT to 21:40UT) outbreak on 3 July 2014 (left panel) and for biomass burning (signal temporally integrated from 19:27UT to 20:48UT) on 19 June 2013 (right panel). The iterative method used a fixed lidar ratio value of S=45sr, determined by climatological measurements (Mona et al., 2006) for the dust aerosol layer. For the biomass burning we used the averaged value of S=63sr obtained from MUSA Raman lidar.

758

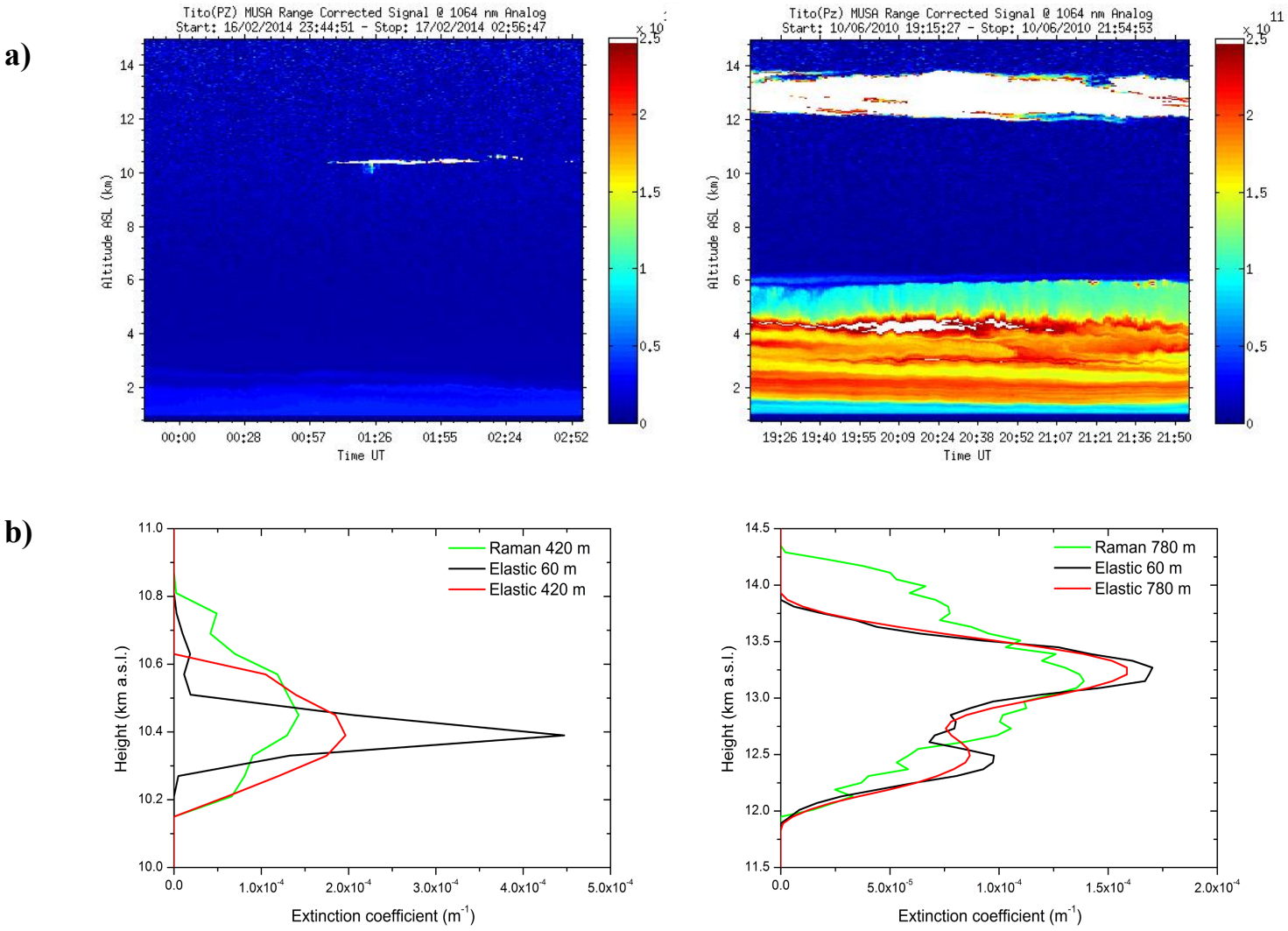

759 Figure 2: a) composite plot of the range corrected signal at 1064nm showing a thin cirrus cloud at about 10km
760 (right panel) and an opaque cirrus cloud at about 12.5 km. b) left panel: lidar extinction profiles at 355nm
761 from Raman and elastic channel respectively a cirrus cloud on 17 February 2014 (signal temporally integrated
762 from 01:29UT to 02:13UT). The iterative method at the two different resolutions (60m and 420m) used a
763 fixed S value (*25sr*), determined by climatological measurement. Figure 2a, b) right panels: same as Figure
764 2a, b) left panels but for a cirrus cloud detected on 10 June 2016 (signal temporally integrated from 19:42UT
765 to 20:44UT). The Raman lidar channel is smoothed over a 420m and 780m spatial window. On 10 June
766 2016, the elastic channel is retrieved using MPLNET algorithm (Lewis et al., 2016) with *S=25sr* at 60m and
767 780m respectively.

768

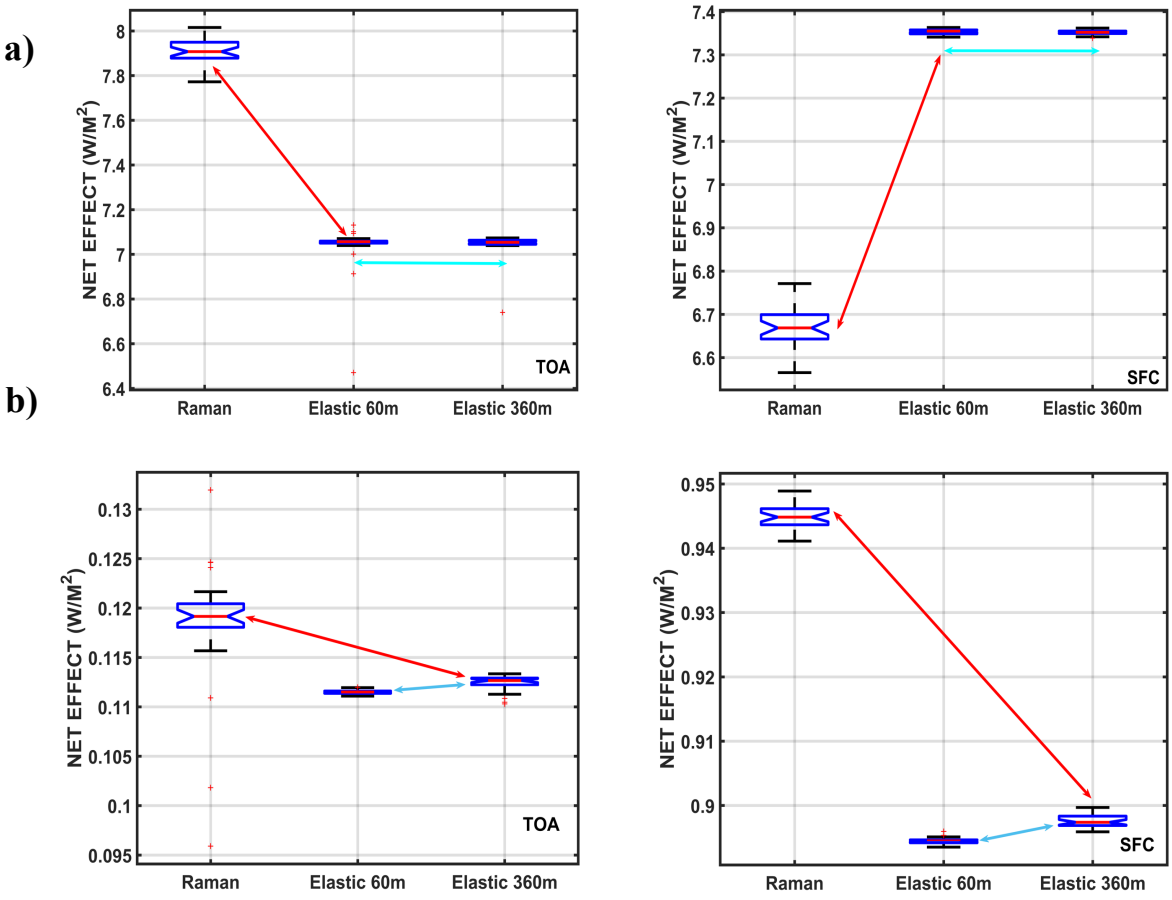

Figure 3. The direct radiative effect, for the dust aerosol case study (Figure 3a) on 03 July 2014 and biomass burning case on 19 June 2013 (Figure 3b) computed for retrievals obtained with Raman lidar channel smoothed over a window of 360m, elastic channel at full resolution (60m) and elastic channel smoothed over a 360m window to be compared with Raman channel . The results are represented as a distribution of values obtained with the MonteCarlo simulations by the boxplots, is calculated at TOA (left panel) and SFC (right panel) respectively. As it is clearly visible, the larger discrepancy in forcing is related mostly to the lidar measurements technique (red arrows), not on the data processing constraints/assumptions (blue arrows).

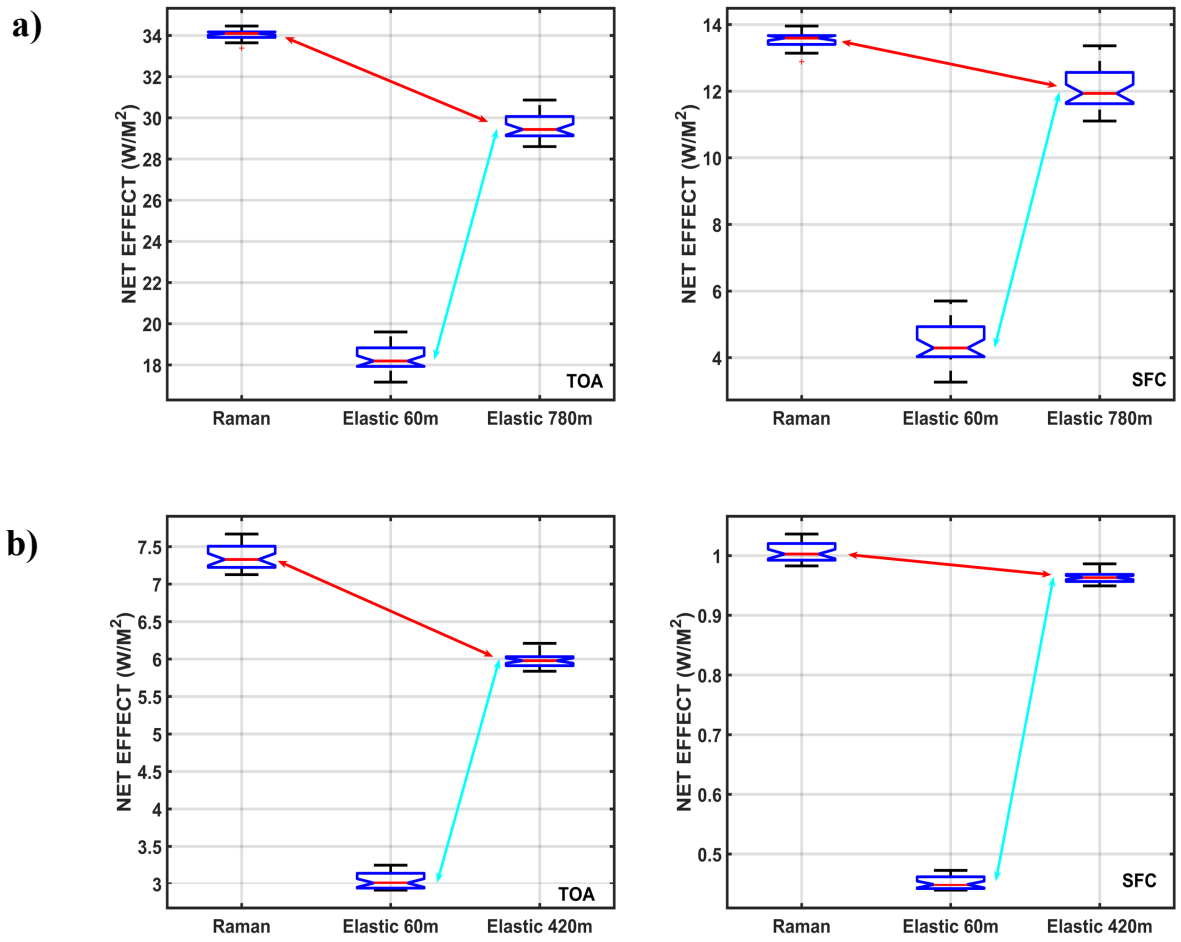

793 Figure 4 Same as Figure 3 but for two cirrus cloud cases (Fig. 4a, 17 Feb 2014, Fig 4b, 10 June 2016).
794 The Raman lidar channel is smoothed over 420m window for cirrus on 17 Feb. 2014 and 780m window
795 for cirrus on 10 June 2010. The net radiative effect is calculated at TOA (left panel) and SFC (right
796 panel) respectively. As it is clearly visible, in both cases the larger discrepancy in radiative effect is
797 related mostly to the data processing (blue arrows), not on lidar technique (red arrows).